REPORT
doi:10.26443/seismica.v5i1.2056
SEISMICA

SubRidge: a Subduction-to-Ridge Model with Synthetic Seismic Waveforms for Benchmarking

Francesco Rappisi * [1], **Manuele Faccenda** [2], **Michael Witek** [3], **Sung-Joon Chang** [4], **Ana MG Ferreira** [5,6]

[1]European Center for Geodynamics and Seismology, Walferdange, 7256, Luxembourg, [2]Department of Geoscience, University of Padua, Padova, 35131, Italy, [3]XCP-2 Eulerian Codes, Los Alamos National Laboratory, Los Alamos, NM, 87545, [4]Department of Geophysics, Kangwon National University, Chuncheon 24341, South Korea, [5]Department of Earth Science, University College London, London WC1E 6BT, United Kingdom, [6]CERIS, Instituto Superior Técnico, Universidade de Lisboa, 1049-001 Lisboa, Portugal

Author contributions: *Conceptualization*: F. Rappisi, A.M.G. Ferreira. *Methodology*: F. Rappisi, M. Faccenda, A.M.G. Ferreira. *Software*: F. Rappisi, M. Faccenda. *Validation*: F. Rappisi, M. Witek. *Resources*: A.M.G. Ferreira, M. Faccenda, S.-J. Chang. *Writing - Original draft*: F. Rappisi. *Writing - Review & Editing*: A.M.G. Ferreira, M. Faccenda, S-J Chang, M. Witek. *Visualization*: F. Rappisi. *Supervision*: A.M.G. Ferreira, M. Faccenda, S-J Chang.

Abstract We present a geodynamic model that simulates the co-evolution of a mid-ocean ridge and adjacent subduction zones. From the dynamic evolution of this system, we derive spatially variable 21 elastic constants and generate a suite of synthetic seismic waveforms. These data are designed to support a wide range of benchmarking and exploratory applications in geophysics and seismology, including (but not limited to) seismic tomography methods (e.g., travel-time and full-waveform inversion), sensitivity analyses of anisotropy, and studies of wave propagation and imaging artifacts under controlled conditions. These waveforms capture key features of upper mantle dynamics, including the effects of anisotropy, slab geometry, and mantle heterogeneity on wave propagation. The dataset includes diverse source-receiver configurations, allowing users to tailor tests to their specific applications and research objectives. By combining a dynamically consistent geodynamic model with synthetic seismograms, this work provides a robust and flexible resource for developing, testing, and evaluating geophysical methods.

Production Editor:
Gareth Funning
Handling Editor:
Anant Hariharan
Copy & Layout Editor:
Mengjie Zheng

Received:
October 6, 2025
Accepted:
May 30, 2026
Published:
June 12, 2026

Non-technical summary This work presents a model of Earth's interior where a mid-ocean ridge and nearby subduction zones evolve together. From this model, we calculate a large set of synthetic seismograms, similar to recordings from real earthquakes. This dataset can help researchers test and improve new methodologies by providing a controlled reference that includes features such as slabs, mantle flow, and anisotropy. The model and dataset are freely available, offering a shared resource for the geoscience community.

1 Introduction

Synthetic models and datasets play a pivotal role in geophysics by providing benchmarks for evaluating, testing and comparing analytical methods within controlled environments. Benchmark models such as Marmousi and Marmousi-2 (Brougois et al., 1990; Versteeg, 1994; Martin et al., 2002), SEAM (Fehler and Larner, 2008), GO_3D_OBS (Górszczyk and Operto, 2021), the SCEC models and test suites (e.g., Community Velocity Models - CVMs, and Layer Over Halfspace LOH.1–LOH.3 problems; Kohler et al., 2003; Moczo et al., 2007), as well as the slab geometry models SLAB1.0 and SLAB2.0 (Hayes et al., 2012, 2018), have been widely adopted to benchmark seismic inversion techniques and innovative numerical methods (e.g., Jiménez Tejero et al., 2015; Sajeva et al., 2016; Badger et al., 2023; Hu et al., 2022).

These models are invaluable for assessing imaging resolution and inversion robustness at local, regional and global scale. However, most of these benchmarks rely on simplified representations of elastic properties, most commonly assuming isotropy, despite often exhibiting significant structural complexity. This simplification persists despite extensive observational and experimental evidence showing that Earth materials exhibit significant seismic anisotropy from the crust to the inner core (e.g., Karato et al., 2008; Montagner, 1998). Since anisotropic structure is of significant interest in seismic tomography and critical for understanding mantle convection, mineral fabric development, and plate dynamics (e.g., Long and Becker, 2010; Salimbeni et al., 2018; Wang and Becker, 2019; Zhao et al., 2023; Baccheschi et al., 2024; Rappisi et al., 2025), neglecting anisotropy in benchmark studies may affect the evaluation of inversion performance in settings where seismic observables are sensitive to anisotropic effects. For example, this is supported by previous studies showing that isotropic or simplified anisotropic assumptions (e.g., azimuthal anisotropy) can introduce significant artifacts and velocity biases, including sub-slab low velocity anomalies exceeding ∼1–1.5% and non-unique thermal or compositional interpretations (e.g., Vanderbeek and Faccenda, 2021; Bezada et al., 2016). For this reason, Qin et al. (2008) developed the SPICE mod-

*Corresponding author: francescorappisi@gmail.com

els providing early benchmarks in anisotropic media and global wave propagation. However, SPICE is primarily a global-scale model with synthetic data limited to periods longer than ∼32 seconds, making it unsuitable for benchmarking body-wave tomography or high-resolution imaging.

Traditional benchmarks are not derived from fully coupled geodynamic simulations of Earth's interior evolution, but rather aim to represent geologically plausible and structurally complex media (e.g., Marmousi, GO_3D_OBS; Versteeg, 1994; Górszczyk and Operto, 2021). While highly valuable for imaging studies, they do not explicitly include dynamically consistent links between deformation processes and resulting structures, which may be relevant in contexts where coupled mantle dynamics and seismic observables are of interest. In this context, models such as the one presented here provide a framework to explore the effects of coupled geodynamic evolution and anisotropy on seismic wave propagation. Such models may also allow researchers to test inversion strategies, quantify the emergence of tomographic artifacts, and evaluate the sensitivity of seismic observables to anisotropic parameters under physically plausible scenarios. Similar approaches integrating geodynamic simulations with anisotropy and synthetic waveform analysis have been recently explored (e.g., Di Leo et al., 2014; Kruse et al., 2024), highlighting the relevance of such coupled frameworks for investigating seismic anisotropy in complex tectonic settings.

In this study, we present a geodynamic model featuring a central ridge and two lateral subduction zones (the SubRidge model), paired with a synthetic dataset of seismic waveforms. This configuration represents a geodynamically complex setting, allowing researchers to test geophysical imaging techniques under physically consistent conditions. Twenty-one elastic constants, derived directly from the simulation, are used to generate synthetic waveforms, providing a coherent testbed for method testing. The SubRidge dataset supports periods down to ∼10 seconds and focuses on a tectonically complex regional setting, enabling more detailed investigations of upper mantle and lithospheric structures. Furthermore, SubRidge integrates geodynamically consistent structures with seismic anisotropy grounded in lattice-preferred orientation (LPO) simulations, offering a valuable synthetic framework.

The effectiveness of this model and dataset has already been demonstrated in Rappisi et al. (2024), where they were employed to investigate the limitations of anisotropic seismic tomography, highlighting how factors such as data coverage and regularization can lead to artificial slab thickening and distortions. This example showcases the model's utility in analyzing the impact of methodological choices on seismic imaging results, providing a context representative of a complex, physically consistent subduction–ridge system under controlled modeling conditions for its application.

This work addresses the current lack of publicly available datasets of high-quality synthetic waveforms directly derived from a geodynamic model. By releasing SubRidge as an open-access resource, we aim to foster innovation and collaboration in the geophysical and seismological communities, providing a versatile tool for benchmarking and method development. SubRidge represents a benchmark model that couples a dynamically consistent geodynamic simulation with LPO-derived seismic anisotropy, making it suitable for testing inversion strategies under physically grounded tectonic scenarios.

2 Data Description and development

Detailed information on the initial model setup, constitutive relations, and material parameters is provided in Rappisi et al. (2024). Only a concise summary of the geodynamic configuration and rheological setup is presented here for completeness.

2.1 Geodynamic Model

The geodynamic model SubRidge spans 80° x 40° in the horizontal plane and extends to a depth of ∼ 700 km. It is interpolated to a grid with 801 x 401 x 71 nodes. The model consists of a central ridge flanked by two subduction zones with slab dips of 30° on each side symmetrical with respect to the ridge (Figs. 1 and 2). For simplicity, the geodynamic numerical modeling was performed in 2-D on a subset of the model, specifically the portion extending from the ridge toward the eastern slab. For the subsequent seismic forward modeling, the resulting elastic fields were replicated westward and along the latitudinal direction to construct the final pseudo-3D computational domain described in Section 2.2.1.

Modeling of 2D subduction was performed with a modified version of the code I2VIS (Gerya and Yuen, 2003), which accounts for conservation of mass, momentum, and energy in polar coordinates under the assumption of incompressibility. Computation of the upper mantle fabrics and visualization of the elastic tensor properties have been performed with the ECOMAN software package (Faccenda et al., 2024).

From the ridge to the trench, the model's initial setup is composed by a left plate with age increasing from 0 to 60 Million years (Myr) and an overriding right plate of 20 Myr age. These thermal ages are defined with the Half-Space Cooling Model (HSCM; Turcotte and Schubert, 2014) for a 90 km thick layer, below which a 0.5 K/km adiabatic gradient is imposed. Above the two plates, a 7 km thick and relatively weak oceanic crust (which lubricates the plates' contact at the subduction boundary) is superimposed among with 30 km thick sticky-air layer placed at the top to model the free surface. To facilitate the initiation of subduction, the initial setup includes a ∼ 30° dipping weak zone. This approach is consistent with numerical studies showing that subduction can initiate along pre-existing weak zones in the lithosphere, particularly when they are favorably oriented (e.g., Toth and Gurnis, 1998). Natural tectonic settings, such as STEP (Subduction-Transform Edge Propagator) faults, further suggest that subduction initiation may be associated with the development of dipping shear zones that localize deformation under convergence (Baes et al., 2011), thereby providing a physical motivation for the imposed geometry. The subducting plates move at a velocity of 4 cm/yr, while the right plate remains stationary. The simulation runs for approximately 13 Myr. Free-slip boundary conditions are applied everywhere, except for the lower permeable boundary where we apply external free-slip (Gerya, 2019). A constant T = 1890 K is used for the bottom boundary and a constant T = 273 K is used for the sticky-air layer. The side boundaries are insulating.

A visco-plastic rheology, formulated in terms of deformation invariants (Ranalli, 1995), is employed to describe the mechanical behavior of the mantle. The oceanic crust is modeled using the Plagioclase An_{75} flow law, while mantle deformation includes diffusion, dislocation, and Peierls creep mechanisms combined with pseudo-plastic yielding following a Drucker–Prager criterion (Karato and Wu, 1993; Hedjazian et al., 2017; Katayama and Karato, 2008). The rheological formulation and constitutive relations are identical to those presented in Rappisi et al. (2024), to which the reader is referred for full details and parameter values.

To simulate strain-induced brittle weakening, the friction coefficient is reduced from 0.6 to 0.4 as a function of accumulated plastic strain, whereas a low friction coefficient ($\mu = 0.05$) is prescribed along the crustal interface to facilitate plate decoupling. Effective viscosities are bounded between 10^{18} and 10^{25} Pa·s. The adopted rheological setup reproduces a low-viscosity asthenospheric channel approximately 100–120 km thick, dominated by dislocation creep, consistent with previous geodynamic studies (e.g., Hedjazian et al., 2017; Yang and Faccenda, 2020; Lo Bue et al., 2021, 2022; Kendall et al., 2022).

Seismic anisotropy is incorporated using 21 elastic constants derived from simulations of LPO development. The model is anisotropic down to 700 km depth. The inclusion of LPO-derived seismic anisotropy provides a physically motivated perturbation to the seismic wavefield, which is critical for evaluating inversion sensitivity and imaging artifacts. This has been widely demonstrated in previous studies showing that anisotropy significantly affects seismic observables and can lead to biased or non-unique inversion results when neglected or simplified (e.g., Vanderbeek and Faccenda, 2021; Vanderbeek et al., 2023; Confal et al., 2019; Bezada et al., 2016)

We consider upper mantle aggregates with a volume ratio of olivine:enstatite = 70:30, which represents a harzburgitic composition, sampled on the original 2-D model grid with a regular spacing of 5 km. The strain-induced development of LPO fabrics in these upper mantle aggregates is simulated using the modified version of D-Rex (Kaminski et al., 2004), integrated into the ECOMAN software package (Faccenda et al., 2024). D-Rex is controlled by three main parameters: the nucleation parameter (λ), the grain-boundary mobility (M), and the critical volume fraction for grain-boundary sliding activation (χ), together with the normalized critical resolved shear stresses (nCRSS) for olivine slip systems. Following the parameterization described in Boneh et al. (2015), we adopt $M = 10$, $\lambda = 5$, and $\chi = 0.3$. The nCRSS values are set to $(010)[100] = 1$, $(001)[100] = 2$, $(010)[001] = 3$, and $(100)[001] = \infty$.

The modeled ridge–subduction system is not intended to reproduce a specific tectonic region, but rather to represent an idealized yet geodynamically plausible configuration inspired by large-scale oceanic settings where spreading centers and convergent margins coexist. It captures several first-order features commonly associated with ridge–subduction systems, including localized mantle upwelling beneath the ridge, strong deformation within the mantle wedge and subslab regions, and strain-induced seismic anisotropy linked to mantle flow. At the same time, the model remains intentionally simplified and does not include heterogeneity along the latitudinal direction, fully time-dependent 3-D flow, compositional complexity, or small-scale tectonic structures.

2.2 Seismic Dataset

We compute 52,080 synthetic seismograms, each lasting 60 minutes, recorded by 1302 stations equally spaced 1° apart, from 30 shallow (i.e., ∼10-20 km depth) and 10 deep (i.e., ∼100-600 km depth) events (Fig. 1).

We simulate 40 earthquakes with magnitudes $5 < M_w < 8$ at local and teleseismic distances (up to ∼80° epicentral distance) with respect to the seismic array. Most of the events are placed in correspondence of the two subduction zones and at the ridge. As shown in Fig. 1, 8 events fall at the edges or out of the 80°x40° geodynamic model. However, we note that before performing the seismic forward modeling the model has been enlarged by replicating the external columns of the grid as described in Section 2.2.1, such that all sources are fully contained within the final domain used for the simulations.

We strategically placed receivers to achieve an optimal coverage. The seismic array spans from 72°E to 113°E and from 15°N to 15°S, covering the ridge (80°E) and the eastern slab (105°E). In total, the array comprises 1302 stations, ensuring dense and spatially uniform sampling of the seismic wavefield. However, users can selectively exclude stations to create sparser distributions that better resemble real-world scenarios. A similar approach was adopted in our previous study (Rappisi et al., 2024), where we conducted tests using both the full station network and reduced subsets mimicking more realistic conditions, such as those encountered in oceanic settings, where seismic stations are often limited to a few scattered islands.

2.2.1 Seismological Forward Modeling

The physical and elastic fields derived from the geodynamic modeling (Section 2.1) were replicated westward (to create the western subduction zone) and along the latitudinal (Y) direction to construct the final pseudo-3D computational domain. As a result, the model is laterally homogeneous along the Y direction, such that all structural and physical properties remain invariant and no additional complexity is introduced in the third dimension. This extrusion of the 2-D model provides a controlled framework for seismic forward modeling while preserving the dynamically consistent structure

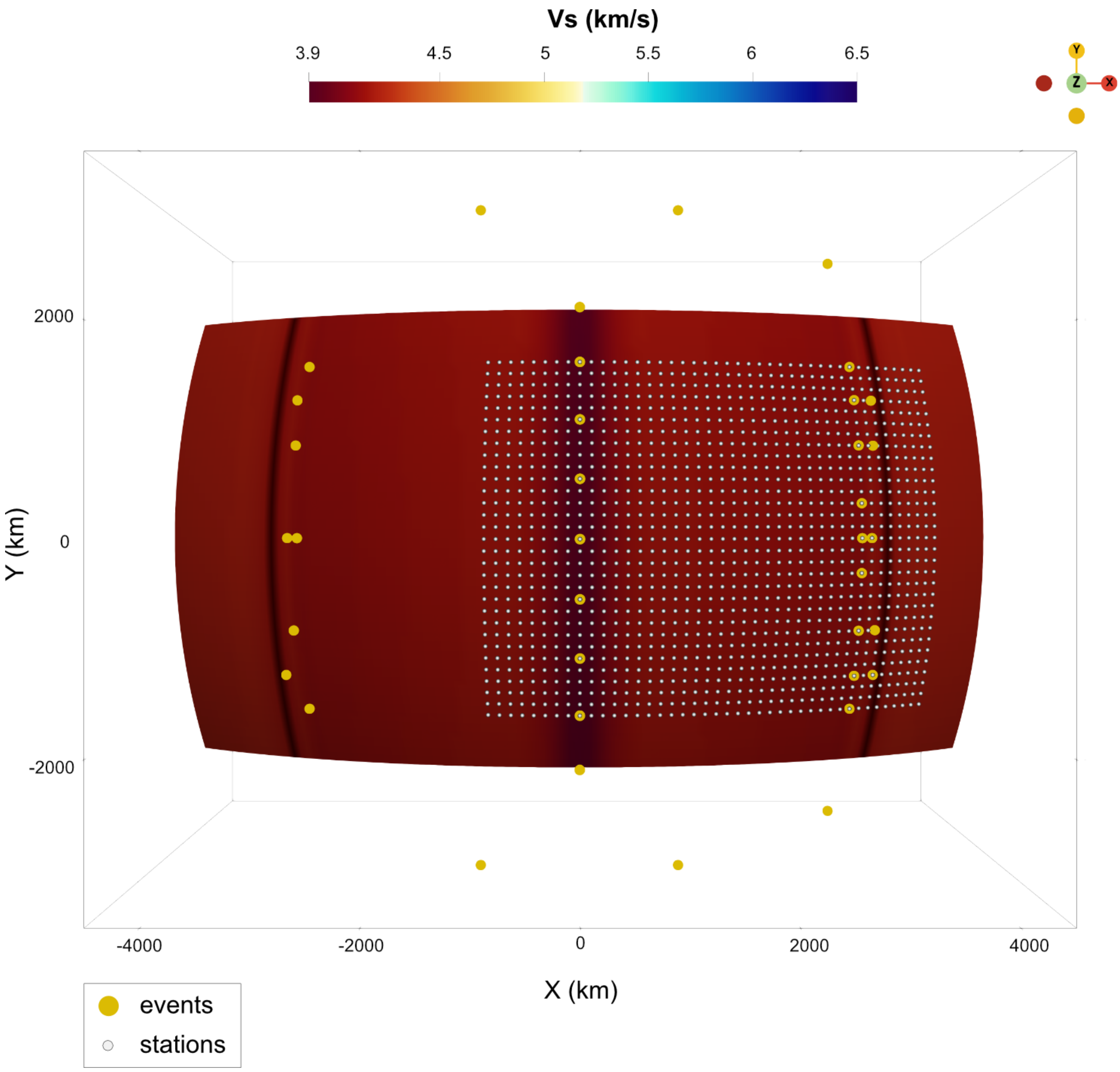

Figure 1 Top-view representation of SubRidge showing the distribution of synthetic earthquake epicenters (yellow dots) and seismic recording stations (white dots). While most seismic sources fall within the model domain, a few epicenters appear outside the current model boundaries. This is due to a later extension of the model in the latitudinal direction, which is discussed in detail in the Section 2.2.1. The present figure reflects the initial configuration prior to this adjustment.

and anisotropy generated by the geodynamic simulation. In this simplified configuration, variations along the latitudinal direction and fully 3-D flow components, such as toroidal mantle circulation, are intentionally neglected in order to isolate the first-order effects of slab geometry, mantle deformation, and anisotropy on seismic wave propagation.

The elastic tensor, represented by 21 independent elastic constants, is interpolated onto an Eulerian grid with a lateral spacing of $\Delta\phi = 0.1^\circ$ and a vertical spacing of $\Delta r = 10$ km. This 2-D grid is then replicated along latitude θ every 0.1° from the equatorial plane within the range of -20° to $+20^\circ$, and reflected across the ridge axis. As a result, the Eulerian domain in coordinates (ϕ, r, θ) spans 80° by 700 km by 40° (*drex_model.xyz* in Section 3). Furthermore, within the spectral element mesher for the calculation of the synthetics, the model has been further enlarged to reach a final dimension of 80° x 700 km x 80° by replicating the external columns of the grid and include all the seismic events. The final 3-D computational domain is characterized by two subduction zones, symmetric with respect to the central oceanic ridge and without variations along the latitudinal direction in elastic properties or anisotropy.

A modified version of SPECFEM3D_GLOBE – based on the spectral element method (SEM; Komatitsch and Tromp, 1999; Chen and Tromp, 2007; Tromp et al., 2008) – was used to simulate seismic wave propagation through the SubRidge geodynamic model presented in the previous section. The SubRidge model was first interpolated onto a depth-variable grid (Aki and Richards, 2002; Dahlen and Tromp, 1998; Sadourny, 1972; Ronchi et al., 1996) where, from the surface, the cell sizes are doubled at each major discontinuity (i.e., Moho, 670 km and core-mantle-boundary, CMB). This resolution is maintained until the next discontinuity, where it is doubled again, and this pattern continues down to the bottom of the model. Fig. 2 illustrates the resulting

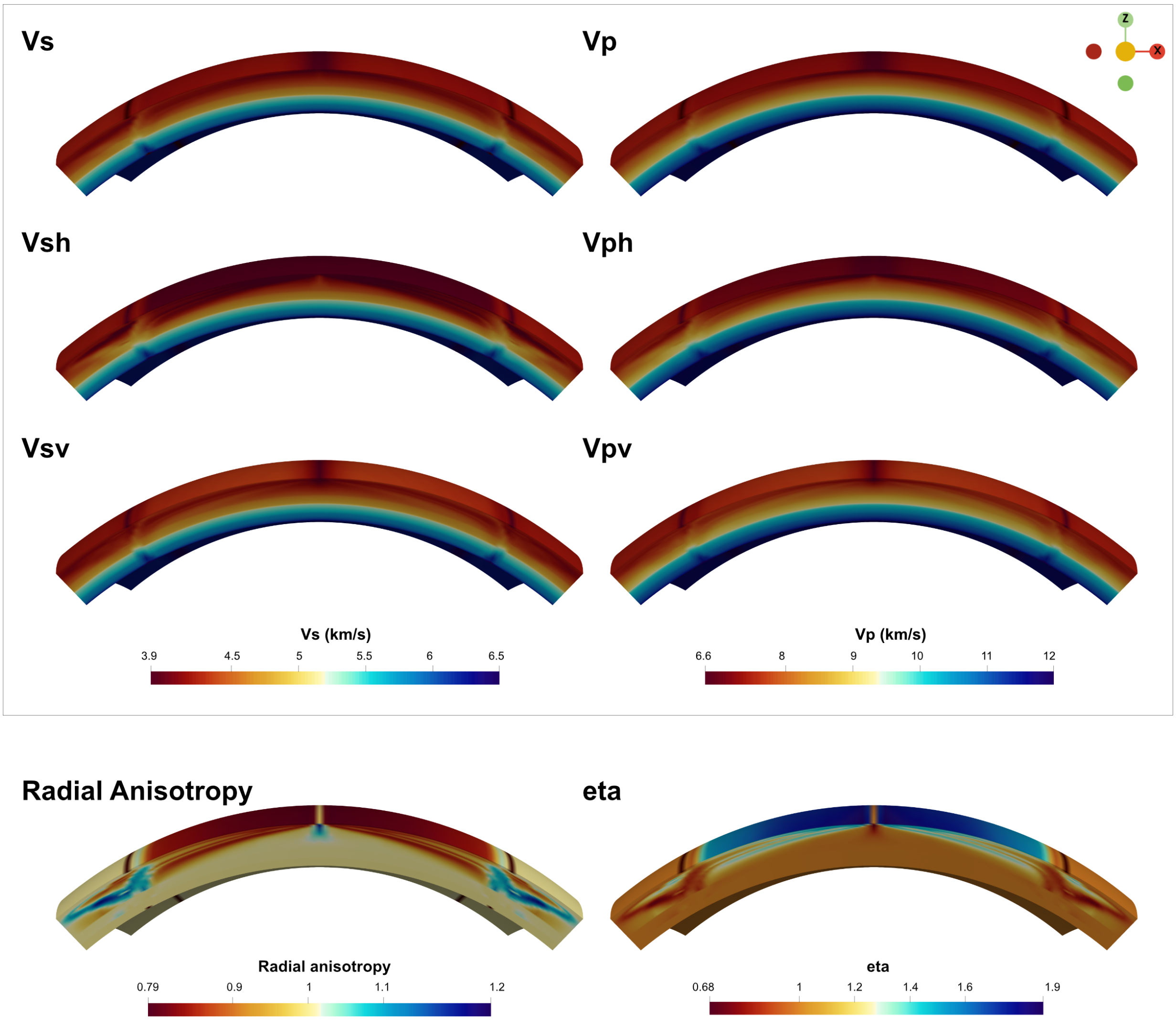

Figure 2 Representation of seismic velocity distributions within the model. The isotropic shear-wave (Vs) and compressional-wave (Vp) velocities are shown alongside the anisotropic components: horizontally and vertically polarized shear-wave velocities (Vsh, Vsv) and compressional-wave velocities (Vph, Vpv). The figure also includes radial anisotropy distribution –expressed as the ratio between horizontal and vertical components ($\frac{V_{SH}^2}{V_{SV}^2}$)– and the anisotropy parameter η (eta), which provides additional insight into the directional dependence of compressional-wave propagation.

spatial distribution of isotropic and anisotropic seismic velocities, including radial anisotropy and the η parameter. Vsh, Vsv, Vph, and Vpv are computed from the anisotropic elastic tensor under the assumption of transverse isotropy with a vertical symmetry axis. The isotropic equivalent velocities (Vp and Vs) are derived from a Voigt-averaged approximation of the full elastic tensor. Radial anisotropy is quantified through the relative difference between horizontal and vertical shear-wave velocities ($\frac{V_{SH}^2}{V_{SV}^2}$). η is computed from the elastic stiffness tensor and used as a scalar measure of azimuthal elastic anisotropy. Fig. 3 provides an example of the synthetic waveforms together with the corresponding source–receiver geometry within the model.

The original SPECFEM3D_GLOBE code was modified to incorporate the density and 21 elastic moduli of the geodynamic model in the depth range $24 \leq z \leq 670$ km. Elsewhere, we use PREM (Dziewoński and Anderson, 1981), and we specify a crustal layer that is characterized by two discontinuities at depths of 14.0 km and 24.4 km with properties identical to those of PREM.

The seismic forward-modeling workflow adopted in this study follows the implementation described in Rappisi et al. (2024). A concise summary of the main steps and simulation parameters is provided here for completeness.

The first step of the forward modeling involves the generation of the calculation mesh. Using the spectral-element mesher, provided within the software package SPECFEM3D_GLOBE, the 3-D domain has been subdivided into n smaller elements or sub volumes. The meshing methodology is based on the cubed-sphere approach of Sadourny (1972) and Ronchi et al. (1996), which divides the globe into six chunks that are further subdivided into mesh slices. Next, we interpolate the elastic tensors –derived from the geodynamic modeling– onto this mesh. Once the mesh is generated, seismic wave propagation is computed using the SPECFEM3D_GLOBE solver, which solves the seismic wave equation in a fully anisotropic medium parameterized by the 21 elastic coefficients derived from the geodynamic model (Aki and Richards, 2002; Dahlen and Tromp, 1998).

Absorbing boundary conditions are applied on the two sides and bottom edges of the spherical chunk. The spectral-element domain is (Φ,R,Θ) = (80° x 6371 km x 80°), with n_ϕ = 384 and n_θ = 192, resulting in a horizontal resolution of ∼0.2° and ∼0.4° along longitude and latitude, respectively. The minimum accurate wave period is T_{min} = ∼10 s, computed as:

$$T_{min} = \frac{256}{n_\phi}\frac{\Phi}{90} \times 17 \approx 10s\,, \tag{1}$$

where Φ is the angular width in degrees. The vertical resolution is determined by the mesher so that its size varies with depth and is doubled at the main discontinuities (i.e. Moho, 670 km and core-mantle boundary, CMB).

For simplicity, attenuation, gravity, ocean, topography and bathymetry effects on seismic wave propagation have been neglected. We store the SEM waveforms in SAC format (Goldstein and Snoke, 2005).

3 Data Access

All files are freely available online at Rappisi (2025a). An overview of the repository is presented in Table 1, with further details provided below:

- The *drex_model.xyz* file, a text file containing the 21 components of the elastic tensors and mesh geometry information describing the elastic and discretization properties of the SubRidge model. The file is organized in rows and columns. Variables, listed in the file, are preceded by the # symbol followed by the name of the variable (e.g., $\#Depth$, $\#Lon$, $\#Lat$, $\#RHO$, $\#C11$, etc.). From the top to the bottom of the .xyz file, we find first the number of nodes along the three directions x, y and z (NX, NY, and NZ, respectively). Then, longitude and latitude are reported in radians. Longitudes span from 0.698 to 2.094 rad, and latitudes span from 1.222 to 1.920 rad. Depths are reported in meters from the deeper to the shallower layers, i.e., from 660,000 to 0 m. The elastic tensors, reported in GPa, are oriented according to a local (or radial) Cartesian reference system where the x-axis points East, y-axis points North and z-axis points up. Density (here referred as $\#RHO$) is reported in Kg/m^3.

- The *STATIONS* file, a text file containing information about station locations, such as latitude, longitude and elevation.

- Subfolder *SEIS*, the directory with the seismic waveforms. It is organized in subdirectories named after the source. The waveforms are provided in SAC format (Goldstein and Snoke, 2005).

- Subfolder *SOURCES*, the directory containing the Centroid Moment Tensors (CMT) solutions for the 40 seismic events. We note that these events are artificial; however they have been created to mimic similar events occurring in similar geological environments, such as ridge or subduction megathrust events.

- Subfolder *matlab scripts*, the directory with matlab scripts for reading and plotting the geodynamic model *drex_model.xyz*. The user can read the elastic tensor component and derive P- or S-wave velocities (both vertical and horizontal components –Vpv, Vph, Vsv, Vsh– or isotropic velocities –Vp,Vs) and the anisotropic parameter η. Furthermore, $read\_drex\_model.mat$ also allows to write the SubRidge model properties (e.g., Vp, Vs, Vpv, Vph, Vsv, Vsh, rho, eta) in .vtk format readable by Paraview (https://www.paraview.org/) through the use of the $vtkwrite.m$ function.

4 Data usage

This dataset was originally introduced and used in Rappisi et al. (2024), where it supported a fully integrated seismo-geodynamical analysis. In that study, synthetic seismic waveforms were generated from a geodynamic model representing ridge-to-slab evolution and then inverted for isotropic and radially anisotropic Earth structure. The work highlighted how regularization choices and data coverage strongly influence the retrieval of seismic anisotropy, leading to artifacts such as artificial slab thickening and age-independent anisotropy.

Beyond its original application, the SubRidge dataset is intended to support a broad range of benchmark and exploratory investigations across geophysics and computational seismology. Its combined geodynamic and seismic design makes it well suited for:

- **Benchmarking seismic tomography algorithms**, such as full-waveform inversion, travel-time tomography, and adjoint methods. The known ground truth allows rigorous quantification of accuracy, resolution, and the emergence of artifacts, within a controlled synthetic framework based on a 2D geodynamic model extended into a 3D representation.

- **Sensitivity studies**, to explore how different physical parameters (e.g., anisotropy, slab geometry) affect seismic observables such as wave speeds, travel times, or amplitudes.

- **Testing inversion parameterizations**, including comparisons between isotropic vs. anisotropic, elastic constants vs. velocity fields, or even different formulations of anisotropy (e.g., transverse isotropy vs. full 3D).

- **Designing realistic acquisition geometries**, including sparse or uneven station/event distributions that mimic real-world networks (e.g., ocean-bottom arrays, regional deployments).

- **Machine learning and data-driven methods**, where synthetic datasets with known labels are critical for training, benchmarking, and uncertainty quantification.

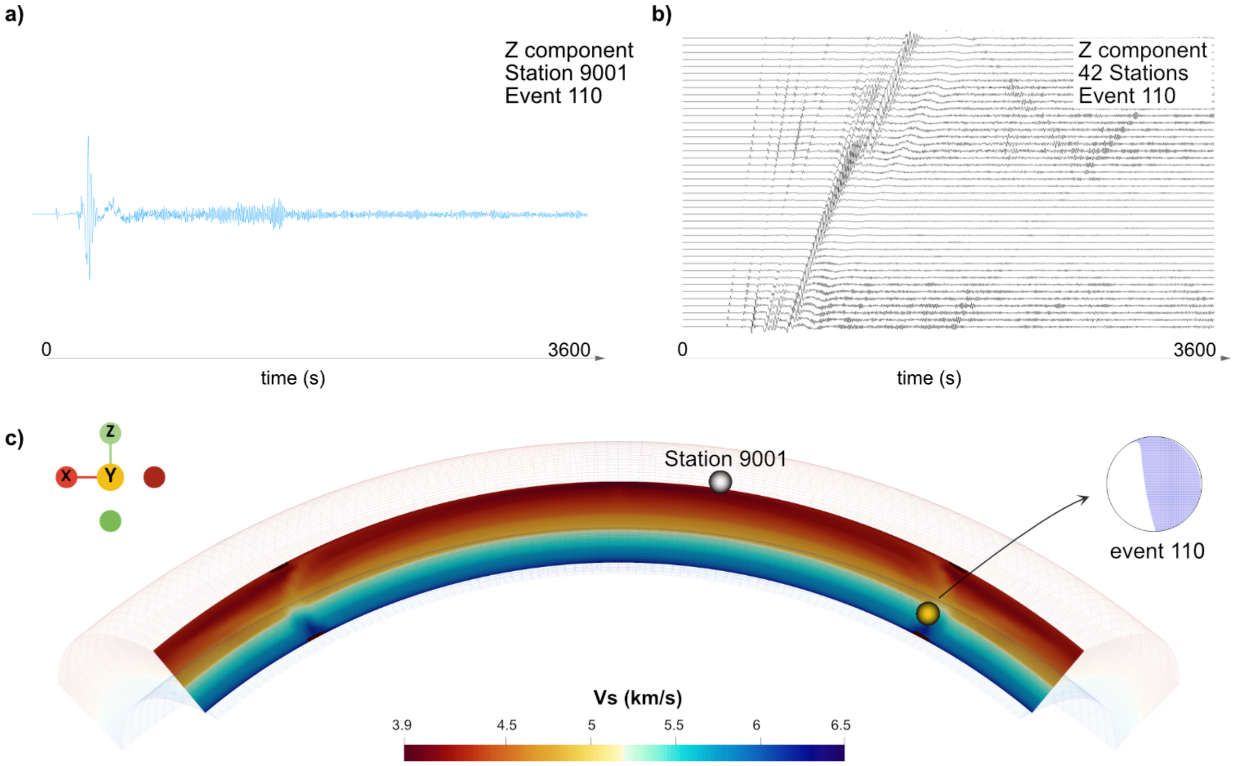

Figure 3 (a) Vertical-component (Z) seismogram recorded at station 9001 from seismic event 110, low-pass filtered at 0.1 Hz and decimated by a factor of 10. (b) Vertical-component (Z) seismograms recorded at 42 stations for seismic event 110, low-pass filtered at 0.1 Hz and decimated by a factor of 10. (c) Corresponding source–receiver configuration for the seismogram shown in panel (a), displayed within the geodynamic model together with an illustrative slice of isotropic shear-wave velocity (Vs) and the focal mechanism of the same seismic event. The figure is shown for illustrative purposes and represents a small subset of the more than 50,000 waveform recordings presented in this study.

Item	Type	Description
drex_model.xyz	text file	SubRidge geodynamic model
STATIONS	text file	seismic stations information
SEIS	folder	synthetic waveforms in SAC format
SOURCES	folder	CMT solutions
Matlab scripts	MATLAB scripts	scripts for reading and plotting SubRidge

Table 1 Dataset Content

- **Educational applications**, including teaching modules on wave propagation, forward modeling, and inversion, where students can interact with a physically grounded yet controllable dataset.

4.1 Limitations

The dataset simplifies some physical processes to focus on structural and anisotropic effects. In particular, it omits:

- seismic attenuation (Q), which can significantly affect surface wave amplitudes at the periods considered here (Ruan and Zhou, 2010, 2012; Savage et al., 2010);
- topography, ocean, and gravity effects, including secondary effects such as tilt and compliance noise associated with ocean-bottom processes (Janiszewski et al., 2023);
- scattering due to small-scale heterogeneities, which can introduce stochastic noise and elastic focusing effects (Shearer and Buehler, 2019; Spetzler et al., 2002).

Additionally, although the moment tensors are realistic, the events are synthetic and do not reflect complex rupture processes (e.g., finite source effects). Waveforms are valid and reliable for frequencies up to ∼0.1 Hz (minimum accurate period ∼10 s); above this, numerical dispersion and modeling simplifications may limit their interpretability. Lastly, the 1-hour record length limits the analysis of long-period phases, such as major-arc surface waves and normal modes at large epicentral distances (e.g., >110°), which may arrive outside the simulated time window.

We encourage the reuse and extension of this dataset for algorithm benchmarking, comparative modeling, and cross-disciplinary applications in seismology, geodynamics, and computational Earth sciences. As an open-access benchmark, it is intended to serve both as a foundation for methodological testing and as an initial test for novel investigations.

Data availability

The dataset can be accessed at Rappisi (2025a). The development of seismic anisotropy in upper mantle aggregates was simulated using the D-Rex algorithm, as implemented in the ECOMAN software suite (https://newtonproject.geoscienze.unipd.it/ecoman/; Faccenda et al., 2024). The seismic wavefield simulations in this study were performed using a modified version of the spectral-element code SPECFEM3D_GLOBE. The original version of SPECFEM3D_GLOBE is publicly available via GitHub (https://github.com/geodynamics/specfem3d_globe) and archived on Zenodo (https://doi.org/10.5281/zenodo.7756944). The modified version of SPECFEM3D_GLOBE, used in this work — which enables the use of fully anisotropic Earth models based on 21 independent elastic constants — is available on Zenodo at Rappisi (2025b). All 3D visualizations of the geodynamic models were created using ParaView (https://www.paraview.org/).

References

Aki, K. and Richards, P. G. *Quantitative Seismology*. MIT Press, 2002.

Baccheschi, P., Confal, J., and Pondrelli, S. Splitting intensity tomography to image depth-dependent seismic anisotropy patterns beneath the Italian Peninsula and surrounding regions. *Earth and Planetary Science Letters*, 646:119005, 2024. doi: 10.1016/j.epsl.2024.119005.

Badger, J., Henneking, S., Petrides, S., and Demkowicz, L. Scalable DPG multigrid solver for Helmholtz problems: A study on convergence. *Computers & Mathematics with Applications*, 148: 81–92, 2023. doi: 10.1016/j.camwa.2023.07.006.

Baes, M., Govers, R., and Wortel, R. Subduction initiation along the inherited weakness zone at the edge of a slab: Insights from numerical models. *Geophysical Journal International*, 184(3): 991–1008, 2011. doi: 10.1111/j.1365-246x.2010.04896.x.

Bezada, M., Faccenda, M., and Toomey, D. Representing anisotropic subduction zones with isotropic velocity models: A characterization of the problem and some steps on a possible path forward. *Geochemistry*, 17:3164 – 3189, 2016. doi: 10.1002/2016gc006507.

Boneh, Y., Morales, L. F., Kaminski, E., and Skemer, P. Modeling olivine CPO evolution with complex deformation histories: Implications for the interpretation of seismic anisotropy in the mantle. *Geochemistry, Geophysics, Geosystems*, 16(10): 3436–3455, 2015. doi: 10.1002/2015gc005964.

Brougois, A., Bourget, M., Lailly, P., Poulet, M., Ricarte, P., and Versteeg, R. Marmousi, model and data. In *EAEG workshop-practical aspects of seismic data inversion*, pages cp–108. European Association of Geoscientists & Engineers, 1990. doi: 10.3997/2214-4609.201411190.

Chen, M. and Tromp, J. Theoretical and numerical investigations of global and regional seismic wave propagation in weakly anisotropic earth models. *Geophysical Journal International*, 168(3):1130–1152, 2007. doi: 10.1111/j.1365-246x.2006.03218.x.

Confal, J., Bezada, M., Eken, T., Faccenda, M., Saygin, E., and Taymaz, T. Influence of Upper Mantle Anisotropy on Isotropic P-Wave Tomography Images Obtained in the Eastern Mediterranean Region. *Journal of Geophysical Research: Solid Earth*, 125, 2019. doi: 10.1029/2019jb018559.

Dahlen, F. A. and Tromp, J. *Theoretical Global Seismology*. Princeton University Press, 1998. doi: 10.2307/j.ctv131bvfd.

Di Leo, J., Walker, A., Li, Z.-H., Wookey, J., Ribe, N. M., Kendall, J.-M., and Tommasi, A. Development of texture and seismic anisotropy during the onset of subduction. *Geochemistry, Geophysics, Geosystems*, 15(1):192–212, 2014. doi: 10.1002/2013gc005032.

Dziewoński, A. M. and Anderson, D. L. Preliminary reference Earth model. *Physics of the Earth and Planetary Interiors*, 25:297–356, 1981. doi: 10.1016/0031-9201(81)90046-7.

Faccenda, M., VanderBeek, B. P., de Montserrat, A., Yang, J., Rappisi, F., and Ribe, N. ECOMAN: an open-source package for geodynamic and seismological modelling of mechanical anisotropy [Software]. *Solid Earth*, 15(10):1241–1264, 2024. doi: 10.5194/se-15-1241-2024.

Fehler, M. and Larner, K. SEG advanced modeling (SEAM): Phase I first year update. *The Leading Edge*, 27(8):1006–1007, 2008. doi: 10.1190/1.2967551.

Gerya, T. *Introduction to numerical geodynamic modelling*. Cambridge University Press, 2019. doi: 10.1017/9781316534243.

Gerya, T. and Yuen, D. A. Characteristics-based marker-in-cell method with conservative finite-differences schemes for modeling geological flows with strongly variable transport properties. *Physics of the Earth and Planetary Interiors*, 140(4):293–318, 2003. doi: 10.1016/j.pepi.2003.09.006.

Goldstein, P. and Snoke, A. SAC availability for the IRIS Community. *Incorporated Institutions for Seismology Data Management Center Electronic Newsletter*, 7(1), 2005.

Górszczyk, A. and Operto, S. GO_3D_OBS: the multi-parameter benchmark geomodel for seismic imaging method assessment and next-generation 3D survey design (version 1.0). *Geoscientific Model Development*, 14(3):1773–1799, 2021. doi: 10.5194/gmd-14-1773-2021.

Hayes, G. P., Wald, D. J., and Johnson, R. L. Slab1. 0: A three-dimensional model of global subduction zone geometries. *Journal of Geophysical Research: Solid Earth*, 117(B1), 2012. doi: 10.1029/2011jb008524.

Hayes, G. P., Moore, G. L., Portner, D. E., Hearne, M., Flamme, H., Furtney, M., and Smoczyk, G. M. Slab2, a comprehensive subduction zone geometry model. *Science*, 362(6410):58–61, 2018. doi: 10.1126/science.aat4723.

Hedjazian, N., Garel, F., Rhodri Davies, D., and Kaminski, E. Age-independent seismic anisotropy under oceanic plates explained by strain history in the asthenosphere. *Earth and Planetary Science Letters*, 460:135–142, 2017. doi: 10.1016/j.epsl.2016.12.004.

Hu, Z., Olsen, K. B., and Day, S. M. Calibration of the near-surface seismic structure in the SCEC community velocity model version 4. *Geophysical Journal International*, 230(3):2183–2198, 2022. doi: 10.1093/gji/ggac175.

Janiszewski, H. A., Eilon, Z., Russell, J., Brunsvik, B., Gaherty, J., Mosher, S., Hawley, W., and Coats, S. Broad-band ocean bottom seismometer noise properties. *Geophysical Journal International*, 233(1):297–315, 2023. doi: 10.1093/gji/ggac450.

Jiménez Tejero, C., Dagnino, D., Sallarès, V., and Ranero, C. R. Comparative study of objective functions to overcome noise and bandwidth limitations in full waveform inversion. *Geophysical Journal International*, 203(1):632–645, 2015. doi: 10.1093/gji/ggv288.

Kaminski, E., Ribe, N. M., and Browaeys, J. T. D-Rex, a program for calculation of seismic anisotropy due to crystal lattice preferred orientation in the convective upper mantle. *Geophysical Journal International*, 158(2):744–752, 2004. doi: 10.1111/j.1365-246x.2004.02308.x.

Karato, S.-i. and Wu, P. Rheology of the upper mantle: A synthesis. *Science*, 260(5109):771–778, 1993. doi: 10.1126/science.260.5109.771.

Karato, S.-i., Jung, H., Katayama, I., and Skemer, P. Geodynamic significance of seismic anisotropy of the upper mantle: New insights from laboratory studies. *Annu. Rev. Earth Planet. Sci.*, 36: 59–95, 2008. doi: 10.1146/annurev.earth.36.031207.124120.

Katayama, I. and Karato, S.-i. Low-temperature, high-stress deformation of olivine under water-saturated conditions. *Physics of the Earth and Planetary Interiors*, 168:125–133, 2008. doi: 10.1016/j.pepi.2008.05.019.

Kendall, E., Faccenda, M., Ferreira, A., and Chang, S.-J. On the relationship between oceanic plate speed, tectonic stress, and seismic anisotropy. *Geophysical research letters*, 49(15): e2022GL097795, 2022. doi: 10.1029/2022gl097795.

Kohler, M., Magistrale, H., and Clayton, R. Mantle heterogeneities and the SCEC reference three-dimensional seismic velocity model version 3. *Bulletin of the Seismological Society of America*, 93(2):757–774, 2003. doi: 10.1785/0120020017.

Komatitsch, D. and Tromp, J. Introduction to the spectral element method for three-dimensional seismic wave propagation. *Geophysical journal international*, 139(3):806–822, 1999. doi: 10.1046/j.1365-246x.1999.00967.x.

Kruse, J. P., Rümpker, G., Link, F., Duretz, T., and Schmeling, H. Anisotropy and XKS splitting from geodynamic models of double subduction: testing the limits of interpretation. *Geophysical Journal International*, 239(3):1400–1424, 2024. doi: 10.1093/gji/ggae328.

Lo Bue, R., Faccenda, M., and Yang, J. The role of Adria plate lithospheric structures on the recent dynamics of the Central Mediterranean region. *Journal of Geophysical Research: Solid Earth*, page e2021JB022377, 2021. doi: 10.1029/2021JB022377.

Lo Bue, R., Rappisi, F., Vanderbeek, B. P., and Faccenda, M. Tomographic Image Interpretation and Central-Western Mediterranean-Like Upper Mantle Dynamics From Coupled Seismological and Geodynamic Modeling Approach. *Frontiers in Earth Science*, 10:884100, 2022. doi: 10.3389/feart.2022.884100.

Long, M. D. and Becker, T. W. Mantle dynamics and seismic anisotropy. *Earth and planetary science letters*, 297(3-4): 341–354, 2010. doi: 10.1016/j.epsl.2010.06.036.

Martin, G. S., Larsen, S., and Marfurt, K. Marmousi-2: An updated model for the investigation of AVO in structurally complex areas. In *SEG International Exposition and Annual Meeting*, pages SEG–2002. SEG, 2002. doi: 10.1190/1.1817083.

Moczo, P., Kristek, J., Galis, M., Pazak, P., and Balazovjech, M. The finite-difference and finite-element modeling of seismic wave propagation and earthquake motion. *Acta physica slovaca*, 57 (2), 2007. doi: 10.2478/v10155-010-0084-x.

Montagner, J.-P. Where can seismic anisotropy be detected in the Earth's mantle? In boundary layers... *Pure and Applied Geophysics*, 151(2):223–256, 1998. doi: 10.1007/s000240050113.

Qin, Y., Capdeville, Y., Maupin, V., Montagner, J.-P., Lebedev, S., and Beucler, E. SPICE benchmark for global tomographic methods. *Geophysical Journal International*, 175(2):598–616, 2008. doi: 10.1111/j.1365-246x.2008.03904.x.

Ranalli, G. *Rheology of the Earth*. Springer Dordrecht, 1995.

Rappisi, F. SubRidge: a 3-D Subduction-to-Ridge Model with Synthetic Seismic Waveforms for Benchmarking [Data set], Zenodo, July 2025a. doi: 10.5281/zenodo.16634304.

Rappisi, F. Modified version of SPECFEM3D_GLOBE supporting external fully anisotropic models, Oct. 2025b. doi: 10.5281/zenodo.17341802.

Rappisi, F., Witek, M., Faccenda, M., Ferreira, A., and Chang, S.-J. Artificial age-independent seismic anisotropy, slab thickening and shallowing due to limited resolving power of (an) isotropic tomography. *Geophysical Journal International*, 237 (1):217–234, 2024. doi: 10.1093/gji/ggae042.

Rappisi, F., Lo Bue, R., Vanderbeek, B., Confal, J., Erman, C., Baccheschi, P., Pondrelli, S., Eken, T., Yolsal-Çevikbilen, S., and Faccenda, M. 3-D mantle flow and structure of the Mediterranean from combined P-wave and splitting intensity anisotropic tomography. *Journal of Geophysical Research: Solid Earth*, 130(6): e2024JB030883, 2025. doi: 10.1029/2024jb030883.

Ronchi, C., Iacono, R., and Paolucci, P. S. The "cubed sphere": A new method for the solution of partial differential equations in spherical geometry. *Journal of computational physics*, 124(1): 93–114, 1996. doi: 10.1006/jcph.1996.0047.

Ruan, Y. and Zhou, Y. The effects of 3-D anelasticity (Q) structure on surface wave phase delays. *Geophysical Journal International*, 181(1):479–492, 2010. doi: 10.1111/j.1365-246x.2010.04514.x.

Ruan, Y. and Zhou, Y. The effects of 3-D anelasticity (Q) structure on surface wave amplitudes. *Geophysical Journal International*, 189(2):967–983, 2012. doi: 10.1111/j.1365-246x.2011.05356.x.

Sadourny, R. Conservative finite-difference approximations of the primitive equations on quasi-uniform spherical grids. *Monthly Weather Review*, 100(2):136–144, 1972. doi: 10.1175/1520-0493(1972)100<0136:cfaotp>2.3.co;2.

Sajeva, A., Aleardi, M., Stucchi, E., Bienati, N., and Mazzotti, A. Estimation of acoustic macro models using a genetic full-waveform inversion: Applications to the Marmousi model. *Geophysics*, 81 (4):R173–R184, 2016. doi: 10.1190/geo2015-0198.1.

Salimbeni, S., Malusà, M. G., Zhao, L., Guillot, S., Pondrelli, S., Margheriti, L., Paul, A., Solarino, S., Aubert, C., Dumont, T., et al. Active and fossil mantle flows in the western Alpine region unravelled by seismic anisotropy analysis and high-resolution P wave tomography. *Tectonophysics*, 731:35–47, 2018. doi: 10.1016/j.tecto.2018.03.002.

Savage, B., Komatitsch, D., and Tromp, J. Effects of 3D attenuation on seismic wave amplitude and phase measurements. *Bulletin of the Seismological Society of America*, 100(3):1241–1251, 2010. doi: 10.1785/0120090263.

Shearer, P. M. and Buehler, J. Imaging upper-mantle structure under USArray using long-period reflection seismology. *Journal of Geophysical Research: Solid Earth*, 124(9):9638–9652, 2019. doi: 10.1029/2019JB017326.

Spetzler, J., Sivaji, C., Nishizawa, O., and Fukushima, Y. A test of ray theory and scattering theory based on a laboratory experiment using ultrasonic waves and numerical simulation by finite-difference method. *Geophysical Journal International*, 148(2):165–178, 2002. doi: 10.1046/j.1365-246x.2002.01001.x.

Toth, J. and Gurnis, M. Dynamics of subduction initiation at preexisting fault zones. *Journal of Geophysical Research: Solid Earth*, 103(B8):18053–18067, 1998. doi: 10.1029/98jb01076.

Tromp, J., Komatitsch, D., and Liu, Q. Spectral-element and adjoint methods in seismology. *Communications in Computational Physics*, 3(1):1–32, 2008. doi: 10.4208/cicp.2008.v3.p1.

Turcotte, D. and Schubert, G. Geodynamics, 160–228, 263–334, 425–463, 2014. doi: 10.1017/cbo9780511843877.

Vanderbeek, B. and Faccenda, M. Imaging upper mantle anisotropy with teleseismic P-wave delays: insights from tomographic reconstructions of subduction simulations. *Geophysical Journal International*, 2021. doi: 10.1093/gji/ggab081.

Vanderbeek, B., Lo Bue, R., Rappisi, F., and Faccenda, M. Imaging upper mantle anisotropy with travel-time and splitting intensity observations from teleseismic shear waves: Insights from tomographic reconstructions of subduction simulations. *Geophysical Journal International*, 2023. doi: 10.1093/gji/ggad389.

Versteeg, R. The Marmousi experience: Velocity model determination on a synthetic complex data set. *The Leading Edge*, 13(9): 927–936, 1994. doi: 10.1190/1.1437051.

Wang, W. and Becker, T. W. Upper mantle seismic anisotropy as a constraint for mantle flow and continental dynamics of the North American plate. *Earth and Planetary Science Letters*, 514: 143–155, 2019. doi: 10.1016/j.epsl.2019.03.019.

Yang, J. and Faccenda, M. Intraplate volcanism originating from upwelling hydrous mantle transition zone. *Nature*, 569:88–91, 2020. doi: 10.1038/s41586-020-2045-y.

Zhao, D., Liu, X., Wang, Z., and Gou, T. Seismic anisotropy tomography and mantle dynamics. *Surveys in Geophysics*, 44(4): 947–982, 2023. doi: 10.1007/s10712-022-09764-7.